Walstromite, BaCa$_2$(Si$_3$O$_9$), from Rankinite Paralava within Gehlenite Hornfels of the Hatrurim Basin, Negev Desert, Israel

Arkadiusz Krzątała [1],*, **Biljana Krüger** [2] , **Irina Galuskina** [1] , **Yevgeny Vapnik** [3]
and Evgeny Galuskin [1]

[1] Institute of Earth Sciences, Faculty of Natural Sciences, University of Silesia, Będzińska street 60, 41-200 Sosnowiec, Poland; irina.galuskina@us.edu.pl (I.G.); evgeny.galuskin@us.edu.pl (E.G.)

[2] Institute of Mineralogy and Petrography, University of Innsbruck, Innrain 52, 6020 Innsbruck, Austria; biljana.krueger@uibk.ac.at

[3] Department of Geological and Environmental Sciences, Ben-Gurion University of the Negev, P.O. Box 653, Beer-Sheva 84105, Israel; vapnik@bgu.ac.il

* Correspondence: akrzatala@us.edu.pl

Abstract: Walstromite, BaCa$_2$Si$_3$O$_9$, known only from metamorphic rocks of North America, was found in small veins of unusual rankinite paralava within gehlenite hornfelses of the Hatrurim Complex, Israel. It was detected at two localities—Gurim Anticline and Zuk Tamrur, Hatrurim Basin, Negev Desert. The structure of Israeli walstromite [with $P\bar{1}$ space group and cell parameters a = 6.74874(10) Å, b = 9.62922(11) Å, c = 6.69994(12) Å, α = 69.6585(13)°, β = 102.3446(14)°, γ = 96.8782(11)°, Z = 2, V = 398.314(11) Å^3] is analogous to the structure of walstromite from type locality—Rush Creek, eastern Fresno County, California, USA. The Raman spectra of all tree minerals exhibit bands related to stretching symmetric vibrations of Si-O-Si at 650–660 cm^{-1} and Si-O at 960–990 cm^{-1} in three-membered rings (Si$_3$O$_9$)$^{6-}$. This new genetic pyrometamorphic type of walstromite forms out of the differentiated melt portions enriched in Ba, V, S, P, U, K, Na, Ti and F, a residuum after crystallization of rock-forming minerals of the paralava (rankinite, gehlenite-åkermanite-alumoåkermanite, schorlomite-andradite series and wollastonite). Walstromite associates with other Ba-minerals, also products of the residual melt crystallization as zadovite, BaCa$_6$[(SiO$_4$)(PO$_4$)](PO$_4$)$_2$F and gurimite, Ba$_3$(VO$_4$)$_2$. The genesis of unusual barium mineralization in rankinite paralava is discussed. Walstromite is isostructural with minerals—margarosanite, BaCa$_2$Si$_3$O$_9$ and breyite, CaCa$_2$(Si$_3$O$_9$), discovered in 2018.

Keywords: walstromite; margarosanite; breyite; pseudowollastonite; structure; Raman; paralava; pyrometamorphism; Hatrurim Complex; Israel

1. Introduction

Walstromite, BaCa$_2$(Si$_3$O$_9$), previously known only from metamorphic rocks of North America [1–6], was found in rankinite paralava in two localities of the Hatrurim Basin—the Gurim Anticline area and in the vicinity of Zuk (Cliff) Tamrur (Figure 1). Paralava forms small irregular veins up to 5 cm thickness within gehlenite-larnite (flamite) hornfelses of the Hatrurim Basin (Negev Desert, Israel). The Hatrurim Basin is the biggest outcropping area of pyrometamorphic rocks known as the Hatrurim Complex, Hatrurim Formation or Mottled Zone [7–9]. Paralavas hosted by gehlenite-larnite hornfelses are characterized by a considerable variety of Ba-bearing minerals such as baryte, hashemite, Ba(CrO$_4$); celsian, BaAl$_2$Si$_2$O$_8$; barioferrite, BaFe$_{12}$O$_{19}$; sanbornite, Ba$_2$(Si$_4$O$_{10}$) and fresnoite, Ba$_2$Ti(Si$_2$O$_7$)O. Several Ba-phases are type locality minerals as zadovite, BaCa$_6$[(SiO$_4$)(PO$_4$)](PO$_4$)$_2$F;

aradite, $BaCa_6[(SiO_4)(VO_4)](VO_4)_2F$ [10]; gurimite $Ba_3(VO_4)_4$; hexacelsian, $BaAl_2Si_2O_8$ [11] and bennesherite, $Ba_2Fe^{2+}Si_2O_8$ [12]. Walstromite occurs with other Ba-minerals in small enclaves between large rankinite, gehlenite or garnet crystals.

Walstromite is a ring silicate and the structural analog of the synthetic high-pressure phase "wollastonite-II," $Ca_3(Si_3O_9)$, also referred as "Ca-walstromite" [13–15]. "Ca-walstromite" was recently detected as an inclusion in diamond and described as a new mineral species under the name breyite (IMA2018-062) [16–18]. In addition to walstromite reported in 1964 [1] and breyite, another isostructural mineral is known—Pb-analog of walstromite–margarosanite, $PbCa_2(Si_3O_9)$, common since 1916 [19]. These three minerals belong to the group, which according to the CNMNC-IMA (Commission on New Minerals, Nomenclature and Classification—International Mineralogical Association) rules should be termed as the margarosanite group.

In this paper, we report the data on a new genetic type of walstromite and mineral assemblages and the composition of associated minerals. The genesis of unusual barium mineralization in rankinite paralava is discussed.
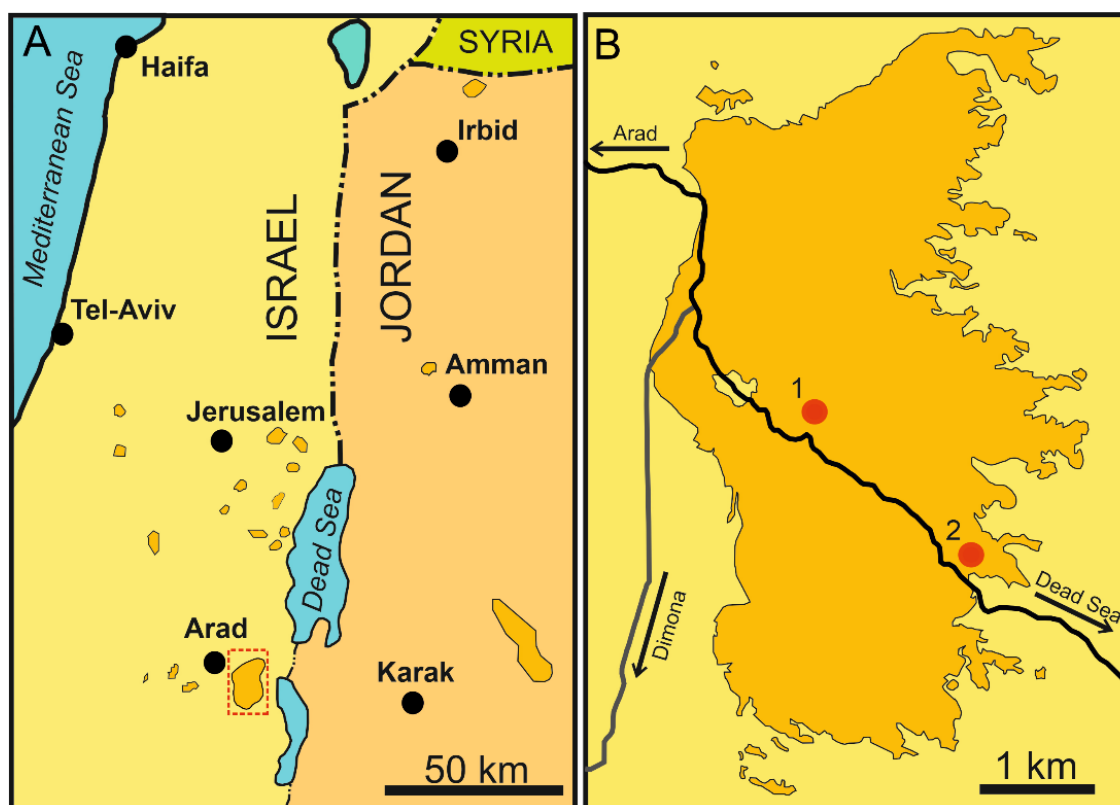

Figure 1. (**A**) Schematic map of the Middle East with outcrops of Hatrurim Complex (dark-yellow). The framed part is magnified in B. (**B**) Schematic map of the Hatrurim Basin. The sampling places of rankinite paralavas are marked by red circles—1. Gurim Anticline, 2. Zuk Tamrur (modified after Reference [20]).

2. Background Information

2.1. Walstromite from the North American Localities

Walstromite was first discovered in sanbornite-bearing metamorphic rocks from the Big Creek, eastern Fresno County, California, USA [1]. Its prismatic 0.2–1.2 cm long crystals have been found commonly as clots and layers of interlocking masses. Some isolated crystals were retrieved from the quartz-rich zones in sanbornite-quartz rocks. Walstromite was found at the few places along the western margin of the North American continent spread from Baja California Norte, Mexico in the

south to the Brooks Range, Alaska in the north. To the south group localities belong—El Rosario and La Madrelena claim, Baja California Norte, Mexico; and in California, the Baumann Prospect, Tulare County; Trumbull Peak, Incline, Mariposa County; and four claims in eastern Fresno County, USA [2–4]. Here, the host rocks are metasediments, formed at a contact of granite and Mesozoic sedimentary rocks. In these localities, walstromite is confined to quartz-sanbornite veins containing a number of common and rare Ba-minerals [2]. In the northern USA, at Gun claim locality and Yukon Territory, Canada, walstromite occurs in contact metasomatic rocks, formed on the contact of Paleozoic limestone and porphyric monzonite stock [2,5,6].

2.2. Hatrurim Complex

This complex is built of high-temperature rocks (sanidinite facies) and products of its low-temperature alteration. Spurrite marbles, larnite rocks and a few varieties of paralava are the most common types of pyrometamorphic rocks of the Hatrurim Complex [7–9,21,22]. Up today, the genesis of these rocks is still debated [23–25]. There is a generally recognized fact, that carbonate protolith of the Hatrurim Complex was subjected to combustion processes [7–9,21]. Hence, two main hypotheses about the genesis of the Hatrurim Complex are currently considered. The first one assumes the burning of organic matters in the bituminous chalk of the Ghareb Formation. As a supporting evidence, can be considered the work of Picard [26] and Minster [27], which indicates that the mean content of organic carbon in the Ghareb Formation rocks is about 15 wt.% in Negev localities [28,29]. The second hypothesis suggests a "mud-volcanic" activity, causing high-temperature pyrometamorphic alteration of primary rocks as a result of methane fire exhaling from tectonic zones of the Dead Sea rift [9,30]. A spontaneous burning of hydrocarbons at the surface is a well-known phenomenon associated with mud volcanism [10,13,30,31].

The occurrence of paralava in the pyrometamorphic rocks of the Hatrurim Complex suggests that combustion processes had to be locally very intense causing partial or bulk melting of the rocks. Pseudowollastonite in some samples of paralava indicates that the temperature could have reached over 1125 °C [32].

2.3. Specific Aspects of Rankinite Paralava

The coarse-grained veins with Ba mineralization occurring within gehlenite hornfelses are classified by Sharygin et al. (2008) [33] as paralava. The main rock-forming minerals of this paralava, apart from rankinite, are wollastonite or pseudowollastonite and minerals of the gehlenite-åkermanite-alumoåkermanite, schorlomite-andradite and fluorapatite-fluorellestadite series. This type of rock has been found at the Negev Desert (Hatrurim Basin, Israel) and Judean Mountains (Nabi Musa, Palestinian Autonomy) [10,11]. Contrary to the traditional definition of paralava, this paralava from the Hatrurim Basin is characterized by the absence of glass and it is fully crystallized rock (Figure 2). The size of some schorlomite-andradite series garnet crystals is up to 1.5 cm in size. These rocks look much more like pegmatite-veins. A growth of large gehlenite, garnet, wollastonite and rankinite crystals elongated sub-perpendicular to the vein walls is common (Figure 2).

Generally, the mineral composition of host gehlenite hornfelses and rankinite paralava is similar. In both types of rocks, the main minerals are Ti-bearing andradite, gehlenite, fluorapatite and accessory magnesiochromite. The hornfelses contain more larnite (flamite), whereas irregularly distributed wollastonite and rankinite are predominant in the paralava (Figure 2). In some cases, rankinite paralava contains both wollastonite and pseudowollastonite [32]. A distinctive feature of this type of paralava is a presence of small aggregates (enclaves) up to 1–2 mm in size enriched in Ba, Ti, P, V, U. The enclaves are composed of rare and recently discovered new minerals, for example, barioferrite, zadovite, aradite, gurimite, vorlanite [10,11,34]. Kalsilite and cuspidine are included in this mineral assemblage. In paralava, commonly garnet and rarely gehlenite and kalsilite crystals host dendritic flamite inclusions, which are interpreted as eutectic intergrowths [35].
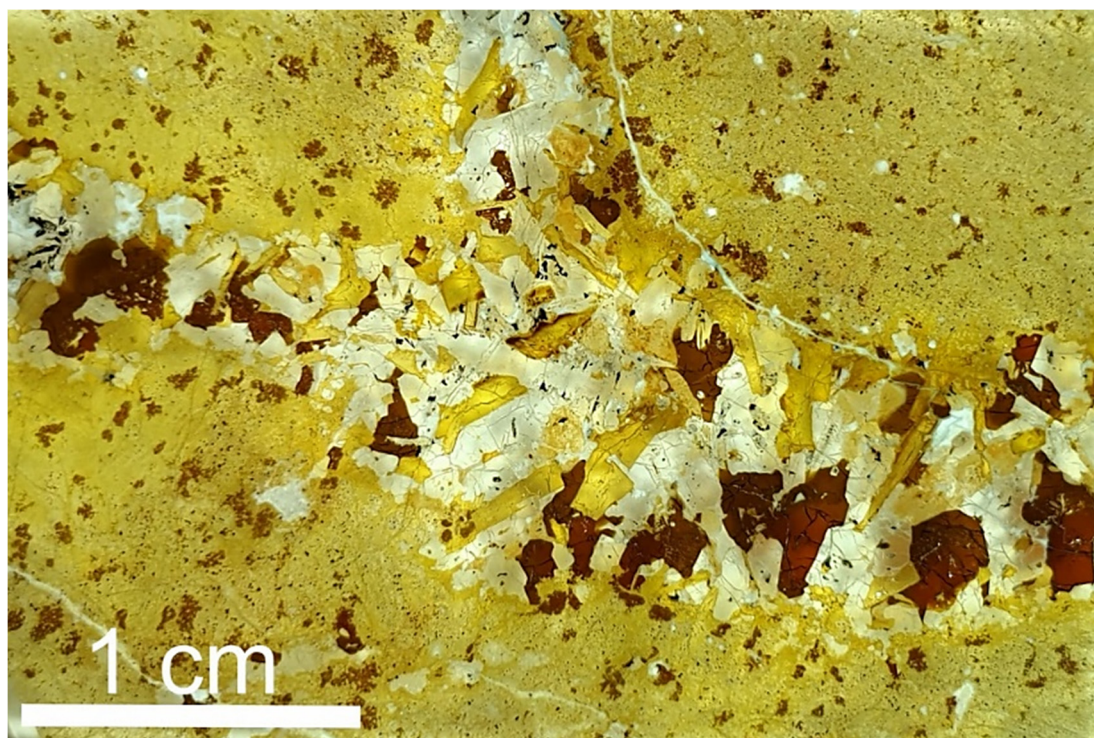
Figure 2. Rankinite paralava in gehlenite hornfels, Gurim anticline (in plane polarized light). Brown: Ti-bearing andradite; yellow of different hues: gehlenite; colorless: rankinite, wollastonite cuspidine and fluorapatite; black: magnesiochromite.

3. Methods

The morphology and composition of walstromite and associated minerals were studied using optical microscopy, scanning electron microscope (Phenom XL, Institute of Earth Sciences, Faculty of Natural Sciences, University of Silesia, Sosnowiec, Poland) and electron microprobe analyzer (Cameca SX100, Institute of Geochemistry, Mineralogy and Petrology, University of Warsaw, Warszawa, Poland). Chemical analyses were carried out (Wavelength-dispersive X-ray spectroscopy (WDS)-mode, 15 keV, 10 nA, ~1 μm beam diameter) using the following lines and standards: Na*Kα*—albite, Si*Kα*, Ca*Kα*, Mg*Kα*—diopside, Al*Kα*, K*Kα*—orthoclase, Ti*Kα*—rutile, Fe*Kα*—Fe_2O_3, Ba*Lα*, S*Kα*—baryte, Sr*Lα*—celestine, Cu*Kα*—cuprite, Zn*Kα*—sphalerite, Ni*Kα*—Ni, Cr*Kβ*—Cr_2O_3, V*Kα*—V_2O_5, P*Kα*—apatite, Zr*Lα*—zircon, Cl*Kα*—tugtupite, F*Kα*—apatite, fluorphlogopite.

Raman spectra of walstromite and associated minerals were recorded on a WITec alpha 300R Confocal Raman Microscope (Institute of Earth Science, Faculty of Natural Sciences, University of Silesia, Sosnowiec, Poland) equipped with an air-cooled solid-state laser (488 nm) and a charge-coupled device (CCD) camera operating at −61 °C. The laser radiation was coupled to a microscope through a single-mode optical fiber with a diameter of 3.5 μm. An air Zeiss LD EC Epiplan-Neofluan DIC-100/0.75NA objective (Carl *Zeiss* AG, Jena, Germany) was used. Raman scattered light was focused on a broadband single-mode fiber with an effective pinhole size of about 30 μm and a monochromator with a 600 mm^{-1} grating was used. The power of the laser at the sample position was ca. 40 mW. Integration times of 3 s with an accumulation of 20 scans and a resolution 3 cm^{-1} were chosen. The monochromator was calibrated using the Raman scattering line of a silicon plate (520.7 cm^{-1}). Spectra processing, such as baseline correction and smoothing, was performed using the SpectraCalc software package GRAMS (Galactic Industries Corporation, Salem, NH, USA). Bands fitting was performed using a Gauss-Lorentz cross-product function, with a minimum number of component bands used for the fitting process.

    Single-crystal X-ray studies of walstromite were carried out with synchrotron radiation, $\lambda = 0.70849$ Å. Diffraction experiments at ambient conditions were performed at the X06DA beamline at the Swiss Light Source (Paul Scherrer Institute, Villigen, Switzerland). The beamline is equipped with a multi-axis goniometer PRIGo [36] and a PILATUS 2M-F detector. The detector was placed 90 mm from the sample, with a vertical offset of 60 mm. For experiments DA+ acquisition software was used [37]. Determination of lattice parameters was done using CrysAlisPro [38]. The crystal structure refinement was performed using the program SHELX-97 [39] implemented in the WinGX software package [40] to an agreement index R1 = 1.86%. As a starting model we used the structure of walstromite reported by [41], ICSD 24426. Further details of data collection and crystal structure refinement are reported in Table 1. Atom coordinates (x, y, z) and equivalent isotropic displacement parameters (Table 2), as well as, anisotropic displacement parameters (Table 3) and selected interatomic distances are shown (Table 4).

Table 1. Crystal data and structure refinement for walstromite.

Crystal Data	
	Walstromite
Crystal system	triclinic
Unit cell dimensions	$a = 6.7487(1)$ $b = 9.6292(1)$ $c = 6.6999(1)$ $\alpha = 69.658(1)°$ $\beta = 102.345(1)°$ $\gamma = 96.878(1)°$
Space group	$P\bar{1}$ no. 2
Volume	398.314 Å^3
Z	2
Density (calculated)	3.717 g/cm^3
Chemical formula sum	$BaCa_2Si_3O_9$
Crystal size (μm)	$50 \times 40 \times 30$
Data Collection	
Diffractometer Detector	beamline PXIII-X06DA, SLS, PILATUS 2M-F
Exposure time/step size	1 s/0.1°
Number of frames	1800
Max. θ°-range for data collection	34.844
Index ranges	$-10 \le h \le 9$ $-11 \le k \le 15$ $-8 \le l \le 9$
No. of measured reflections	3256
No. of unique reflections	2380
No. of observed reflections (I > 2σ (I))	2300

Table 1. *Cont.*

Refinement of the Structure	
no. of parameters	136
R_{int}	0.0062
$R\sigma$	0.0121
$R_1, I > 2\sigma(I)$	0.0186
R_1 all data	0.0190
w$R2$ on ($F2$)	0.0618
GooF	1.134
$\Delta\rho$ min ($-e\text{Å}^{-3}$)	-0.84
$\Delta\rho$ max ($e\text{Å}^{-3}$)	0.95

Table 2. Atom coordinates, U_{eq} (Å^2) values for walstromite.

Site	Atom	*x/a*	*y/b*	*z/c*	*Ueq*	*sof*
Ca1	Ca	0.27471(7)	0.50895(5)	0.76250(8)	0.01546(10)	1
Ca2	Ca	0.43670(7)	0.82840(5)	0.94379(8)	0.01524(10)	1
Ba1	Ba	0.04753(2)	0.84859(2)	0.32124(2)	0.01762(6)	1
Si1	Si	0.09707(10)	0.22164(7)	0.15331(11)	0.01420(13)	1
Si2	Si	0.23400(10)	0.48115(7)	0.28547(12)	0.01431(13)	1
Si3	Si	0.44142(10)	0.19636(7)	0.51338(11)	0.01389(13)	1
O1	O	0.2335(3)	0.2602(2)	−0.0289(3)	0.0170(3)	1
O2	O	−0.1008(3)	0.12162(19)	0.1047(3)	0.0174(3)	1
O3	O	0.0461(3)	0.37101(19)	0.1996(3)	0.0167(3)	1
O4	O	0.3727(3)	0.5564(2)	0.1068(3)	0.0169(3)	1
O5	O	0.1344(3)	0.5858(2)	0.3681(3)	0.0201(4)	1
O6	O	0.3596(3)	0.35601(19)	0.5058(3)	0.0170(3)	1
O7	O	0.6141(3)	0.2340(2)	0.3698(3)	0.0174(3)	1
O8	O	0.5079(3)	0.0916(2)	0.7571(3)	0.0182(3)	1
O9	O	0.2302(3)	0.12399(19)	0.3933(3)	0.0167(3)	1

Table 3. Anisotropic displacement parameters U^{ij} for walstromite.

Site	U^{11}	U^{22}	U^{33}	U^{23}	U^{13}	U^{12}
Ca1	0.0165(2)	0.01433(18)	0.0140(2)	−0.00325(15)	0.00209(17)	0.00079(14)
Ca2	0.01442(19)	0.01699(18)	0.0151(2)	−0.00653(15)	0.00197(17)	0.00151(14)
Ba1	0.01913(8)	0.01579(7)	0.01740(9)	−0.00589(5)	0.00061(6)	0.00260(5)
Si1	0.0131(3)	0.0141(3)	0.0143(3)	−0.0042(2)	0.0015(2)	0.0001(2)
Si2	0.0145(3)	0.0139(3)	0.0146(3)	−0.0046(2)	0.0028(2)	0.0010(2)
Si3	0.0140(3)	0.0145(2)	0.0124(3)	−0.0041(2)	0.0013(2)	0.0009(2)
O1	0.0156(7)	0.0192(7)	0.0168(8)	−0.0059(6)	0.0038(7)	0.0014(6)
O2	0.0137(7)	0.0162(7)	0.0205(8)	−0.0057(6)	0.0007(7)	−0.0008(5)
O3	0.0146(7)	0.0159(7)	0.0195(8)	−0.0070(6)	0.0011(6)	0.0011(5)
O4	0.0169(8)	0.0185(7)	0.0160(8)	−0.0053(6)	0.0054(7)	0.0000(6)
O5	0.0234(9)	0.0180(7)	0.0210(9)	−0.0073(7)	0.0050(8)	0.0046(6)
O6	0.0194(8)	0.0162(7)	0.0154(8)	−0.0057(6)	0.0009(7)	0.0040(6)
O7	0.0174(8)	0.0187(7)	0.0159(8)	−0.0061(6)	0.0031(7)	−0.0008(6)
O8	0.0225(8)	0.0164(7)	0.0133(8)	−0.0038(6)	−0.0003(7)	0.0016(6)
O9	0.0170(7)	0.0156(7)	0.0154(8)	−0.0043(6)	−0.0002(6)	0.0008(5)

Table 4. Selected interatomic distances (Å) for walstromite.

Atom	-atom	Distance (Å)	Atom	-atom	Distance (Å)
Ca1	O1	2.334(2)	Si1	O1	1.600(2)
	O3	2.670(2)		O2	1.594(2)
	O4	2.431(2)		O3	1.660(2)
	O4	2.445(2)		O9	1.676(2)
	O5	2.483(2)		Mean	1.632
	O5	2.853(2)	Si2	O3	1.689(2)
	O6	2.800(2)		O4	1.596(2)
	O7	2.406(2)		O5	1.576(2)
	Mean	2.552		O6	1.680(2)
Ca2	O1	2.362(2)		Mean	1.635
	O2	2.305(2)	Si3	O6	1.676(2)
	O4	2.486(2)		O7	1.597(2)
	O7	2.326(2)		O8	1.592(2)
	O8	2.331(2)		O9	1.681(2)
	O8	2.445(2)		Mean	1.636
	Mean	2.376			
Ba1	O5	2.563(2)			
	O2	2.716(2)			
	O7	2.721(2)			
	O1	2.810(2)			
	O2	2.863(2)			
	O9	2.939(2)			
	O9	3.041(2)			
	O8	3.108(2)			
	O3	3.318(2)			
	O6	3.354(2)			
	Mean	2.943			

4. Results

4.1. Occurrence and Description of Walstromite

In rankinite paralavas from Gurim Anticline and Zuk Tamrur, walstromite occurs with other Ba-minerals in small enclaves between large rankinite, gehlenite or garnet crystals (Figure 3). It generally forms subhedral or anhedral colorless, transparent crystals up to 0.2 mm in size. Rarely can be found poikilitic crystals up to 0.6 mm in size with inclusions of kalsilite and P-bearing flamite (Figure 3). Walstromite, from both localities, has a relatively constant composition (Table 5). The following empirical crystal chemical formulas of walstromite calculated on the basis of 6 cations per formula unit were obtained:

(1) Gurim Anticline: $(Ba_{0.97}Sr_{0.01}Ca_{0.02})_{\Sigma 1.00}(Ca_{2.00}Na_{0.01})_{\Sigma 2.01}(Si_{2.98}Al_{0.01}Ti_{0.01})_{\Sigma 3.00}O_9$,

(2) Zuk Tamrur: $(Ba_{0.95}Sr_{0.01}Ca_{0.02})_{\Sigma 0.98}(Ca_{1.97}Na_{0.02})_{\Sigma 1.99}(Si_{2.99}Ti_{0.02}Al_{0.01})_{\Sigma 3.02}O_9$.

The unique barium-rich minerals were identified in paralava of both localities—celsian, $Ba(Al_2Si_2O_8)$; barioferrite, $BaFe_{12}O_{19}$; gurimite, $Ba_3(VO_4)_2$; minerals of zadovite, $BaCa_6[(SiO_4)(PO_4)](PO_4)_2F$, -aradite, $BaCa_6[(SiO_4)(VO_4)](VO_4)_2F$, series. However, some differences in the chemical composition of the major minerals and the content minor minerals in paralavas of Gurim Anticline and Zuk Tamrur are observed. Bennesherite, $Ba_2FeSi_2O_7$; fresnoite, $Ba_2Ti(Si_2O_7)O$; hexacelsian, $Ba(Al_2Si_2O_8)$; sanbornite, $Ba_2(Si_4O_{10})$ and potentially new mineral—fluorine analogue of alforsite, $Ba_5(PO_4)_3F$, were recognized in paralava from Gurim Anticline [10–12,42]. The accessory minerals of this paralava are vorlanite, khesinite, magnesioferrite, trevorite, dellafossite, tenorite, cuprite, perovskite, hematite and a new mineral—pliniusite, $Ca_5(VO_4)_3F$ [43]. In Gurim Anticline-paralava

nepheline, Ni-bearing magnetite, native copper, as well as sulfides of copper and nickel such as heazlewoodite, chalcocite were found.
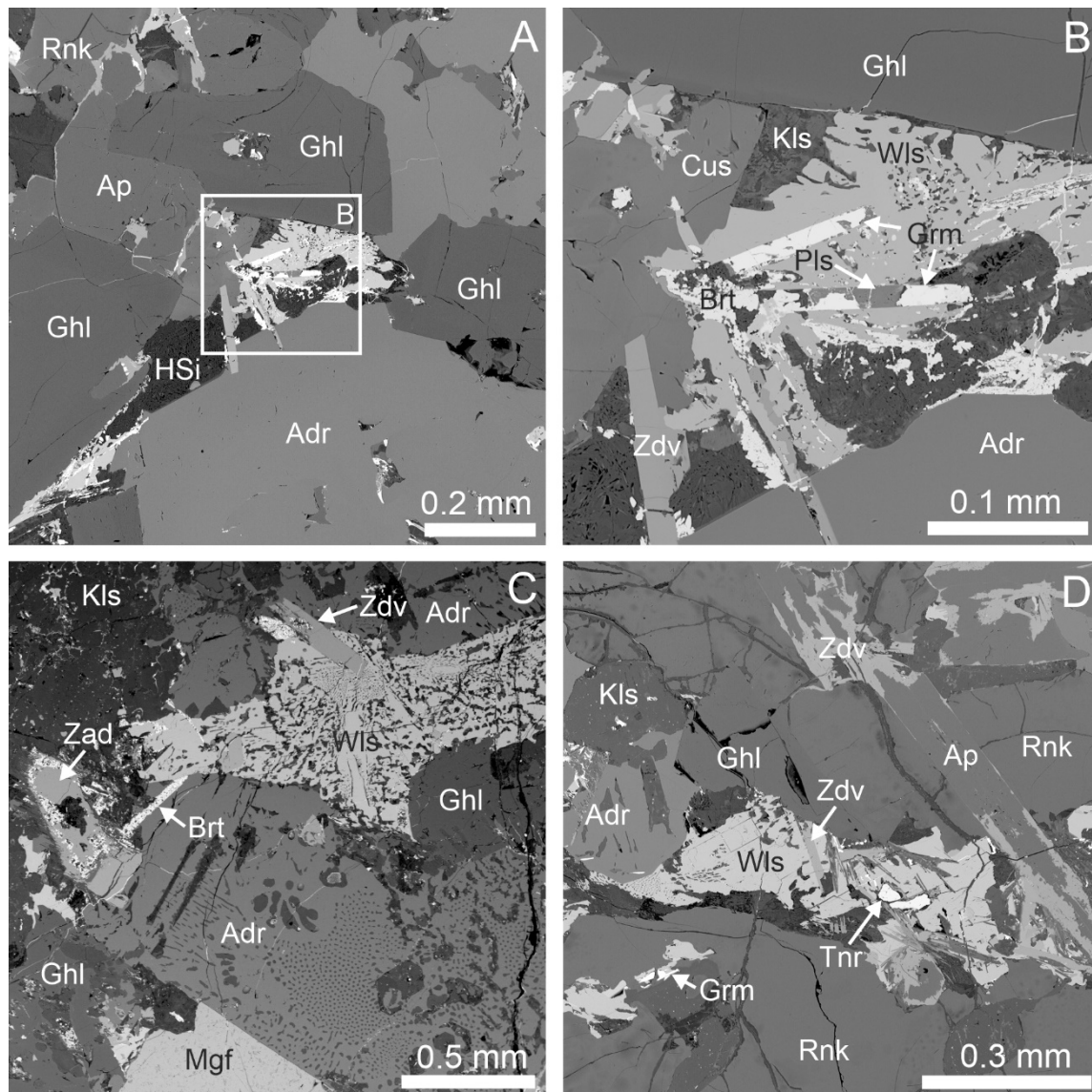

Figure 3. BSE (backscattered electrons) images of paralava with walstromite: (**A**) aggregate of Ba-minerals between large rock-forming minerals of paralava, Zuk Tamrur. Frame shows a fragment magnified in Figure 3B; (**B**) walstromite intergrowing with zadovite and gurimite is partially replaced by pliniusite. Kalsilite, in enclaves containing walstromite, is intensively substituted by a mixture of hydrosilicates and zeolites; (**C**) one of the biggest poikilitic grain of walstromite with kalsilite inclusions and Ti- andradite-flamite (partly altered) eutectoid intergrowth, Zuk Tamrur; (**D**) Euhedral zadovite crystals in walstromite, zadovite partially substituted for fluorapatite, Gurim Anticline. Adr: andradite, Ap: fluorapatite, Brt: baryte, Cus: cuspidine, Ghl: gehlenite, Grm: gurimite, His: hydrosilicate, Pls: pliniusite, Rnk: rankinite, Tnr: tenorite, Wls: walstromite, Zdv: zadovite, Mgf: magnesioferrite, Kls: kalsilite.

Minerals of the melilite group from Zuk Tamrur paralava are varying in composition from alumoåkermanite to gehlenite (Table 6). Every so often, Mg and Na contents are increasing towards the rim of crystals. Mineral with composition $(Ca_{1.45}Na_{0.52}K_{0.02}Sr_{0.02})_{\Sigma 2.01}(Al_{0.47}$ $Fe^{2+}_{0.21}Fe^{3+}_{0.19}Mg_{0.11}Zn_{0.01})_{\Sigma 0.99}(Si_{1.88}Al_{0.12})_{\Sigma 2.00}O_7$ (Table 6, analysis 1) is formally classified as alumoåkermenite. The chemical formula is $(Ca,Na)_2(Al,Mg,Fe^{2+})(Si_2O_7)$ [44], not conforming to

the CNMNC-IMA requirements of the end-member formula. In our opinion, the decision of CNMNC-IMA to approve alumoåkermanite as 50/50 mixture of the two end-members—"soda melilite," $NaCaAlSi_2O_7$ and gehlenite, $Ca_2Al(AlSi)O_7$—was not correct. Therefore this high-sodium melilite from Zuk Tamrur was recalculated on the three main end-members—(1) $NaCa(Al,Fe^{3+})Si_2O_7$–54% ("soda melilite"), (2) $Ca_2(Mg,Fe^{2+})Si_2O_7$ (åkermanite-"ferriåkermanite")–33%, 3) $Ca_2(Al,Fe)(AlSi)O_7$ (gehlenite-"ferroåkermanite")–12% (Table 6, analysis 1). The high-sodium compositions of the "alumoåkermanite " type (Na_2O ~5–6 wt.%) in the studied paralava are rare. Gehlenite with Na_2O impurities about 1–2 wt.% (Table 6; analyses 2, 3) is the most widespread. In paralava from Gurim Anticline more magnesium melilite from åkermanite to magnesium gehlenite with relatively high Fe content is characteristic (Table 6, analyses 4, 5). In melilites from paralava a significant variations Fe^{2+}/Fe^{3+} ratio from ~1 in alumoåkermanite to ~0.1 in gehlenite are noted.

Table 5. Chemical composition of walstromite from Gurim Anticline (1) and Zuk Tamrur (2), wt.%.

	1			**2**		
	n = 15	**s.d.**	**Range**	**n = 5**	**s.d.**	**Range**
TiO_2	0.16	0.10	0–0.34	0.34	0.07	0.24–0.43
SiO_2	40.56	0.40	39.92–41.10	40.19	0.75	39.07–41.10
Al_2O_3	0.15	0.02	0.12–0.19	0.16	0.04	0.12–0.21
BaO	33.62	0.41	32.90–34.26	32.62	0.60	32.18–33.43
SrO	0.27	0.20	0–0.68	0.18	0.11	0.09–0.35
CaO	25.60	0.47	24.84–26.15	24.89	0.39	24.43–25.41
K_2O	0.03	0.02	0–0.06	n.d.		
Na_2O	0.06	0.02	0–0.09	0.15	0.01	0.07–0.11
Total	100.45			98.53		
			Calculated on 9O			
Ba	0.97			0.95		
Sr	0.01			0.01		
Ca	2.02			1.99		
Na	0.01			0.02		
A+B	*3.01*			*2.97*		
Si	2.98			2.99		
Ti^{4+}	0.01			0.02		
Al	0.01			0.01		
T	*2.00*			*3.02*		

Minerals of the garnet supergroup from both localities are presented by andradite, $Ca_3Fe^{3+}_2Si_3O_{12}$, -schorlomite, $Ca_3Ti^{4+}_2Fe^{3+}_2SiO_{12}$, series with an insignificant constituent of hutcheonite, $Ca_3Ti^{4+}_2Al_2SiO_{12}$, end-member (Table 7). In Zuk Tamrur paralava Ti-bearing andradite with high Cr content (Table 7, analysis 3) was detected. In general, central zones of garnets are richer in Ti and Cr where peripherical zones show more Fe.

The rock-forming Ca-silicates (wollastonite, rankinite, cuspidine) in walstromite-bearing paralava exhibit composition close to stoichiometric (Table 8). Raman spectroscopy study of numerous wollastonite grains showed, that pseudowollastonite is absent in the paralava from Zuk Tamrur and Gurim Anticline. Pseudowollastonite is noted many times in rankinite paralava from other localities.

Table 6. Chemical composition of the melilite group minerals from Zuk Tamrur (1–3) and Gurim Anticline (4,5), wt%.

	1	2			3	4			5		
	n = 1	n = 7	s.d	range	n = 4	n = 6	s.d.	range	n = 6	s.d.	range
TiO_2	n.d.	n.d.			0.09	n.d.			n.d.		
SiO_2	39.93	31.67	0.79	30.42–32.80	28.23	37.02	1.31	35.09–38.71	26.26	0.80	25.36–27.09
Fe_2O_3	5.47	7.52	0.42	6.72–8.39	6.30	6.63	0.74	5.67–7.87	5.95	0.33	5.54–6.36
Al_2O_3	10.58	16.11	0.45	15.57–16.91	21.96	10.47	1.24	8.81–12.31	24.77	1.13	23.45–26.22
BaO	0.11	0.13	0.14	0.00–0.34	0.00	1.04	0.48	0.46–1.79	0.00		
SrO	0.59	0.22	0.19	0.00–0.47	0.34	0.69	0.23	0.43–0.96	0.00		
ZnO	0.38	0.63	0.2	0.41–0.89	0.45	0.88	0.12	0.79–0.96	0.00		
NiO	0.00				0.00	0.21	0.1	0.14–0.28	0.00		
FeO *	5.42	1.77	0.36	1.20–2.27	1.31	3.00	0.50	2.27–3.67	0.82	0.23	0.47–1.34
CaO	28.81	35.78	0.51	35.04–36.34	37.35	31.51	0.94	29.96–32.52	38.17	0.08	38.08–38.28
MgO	1.50	2.60	0.54	2.14–3.39	1.57	3.58	0.29	3.20–4.02	1.45	0.27	1.13–1.8
K_2O	0.38	0.36	0.09	0.27–0.50	0.23	0.27	0.08	0.17–0.40	0.29	0.07	0.19–0.37
Na_2O	5.65	1.90	0.3	1.51–2.38	1.25	3.63	0.37	3.42–4.28	0.74	0.10	0.65–0.86
Total	98.81	98.69			99.08	98.93			98.45		
					Calculated on 7O						
Ca	1.45	1.83			1.89	1.61			1.94		
Na	0.52	0.18			0.11	0.34			0.07		
K	0.02	0.02			0.01	0.02			0.02		
Sr	0.02	0.01			0.01	0.02					
Ba						0.02					
A	*2.01*	*2.04*			*2.02*	*2.01*			*2.03*		
Mg	0.11	0.18			0.11	0.25			0.10		
Fe^{2+}	0.21	0.07			0.05	0.12			0.03		
Zn	0.01	0.02			0.02	0.03					
Ni						0.01					
Fe^{3+}	0.19	0.27			0.22	0.24			0.21		
Al	0.47	0.42			0.57	0.35			0.63		
T1	*0.99*	*0.96*			*0.97*	*1.00*			*0.97*		
Al	0.12	0.49			0.66	0.24			0.76		
Si	1.88	1.51			1.34	1.76			1.24		
T2	*2.00*	*2.00*			*2.00*	*2.00*			*2.00*		
Åk	*33*	*28*			*19*	*41*			*14*		
Na-Mel	*54*	*21*			*13*	*36*			*7*		
Ghl	*12*	*51*			*67*	*24*			*79*		

Åk = $Ca_2(Mg,Fe^{2+})Si_2O_7$, Na-mel = $(NaCa)(Al,Fe^{3+})Si_2O_7$, Ghl = $Ca_2Al(AlSi)O_7$, * calculated on charge balance.

Table 7. Chemical composition of garnet from Gurim Anticline (1,2) and Zuk Tamrur (3–5), wt.%.

	1			**2**	**3**	**4**	**5**
	n = 9	s.d.	Range	n = 4	n = 3	n = 2	n = 1
ZrO_2	n.d.			0.20	0.39	n.d.	n.d.
TiO_2	8.64	0.26	8.10–9.06	16.17	11.18	14.32	3.13
SiO_2	28.27	0.25	27.81–28.63	22.41	26.43	24.01	32.65
Fe_2O_3	27.10	0.28	26.78–27.61	25.76	21.54	25.75	28.90
Cr_2O_3	0.19	0.10	0.08–0.40	n.d.	5.64	n.d.	n.d.
V_2O_3	0.16	0.05	0.11–0.24	0.11	n.d.	0.15	0.20
Al_2O_3	2.03	0.06	1.93–2.12	2.26	2.92	2.63	1.42
MgO	0.11	0.02	0.09–0.14	0.10	0.09	0.11	0.08
CaO	32.32	0.15	32.11–32.51	32.22	32.66	32.31	32.65
Total	98.82			99.23	100.85	99.28	99.03
			Calculated on 8O				
Ca	2.99			3.02	2.97	3.00	2.99
Mg	0.02			0.01	0.01	0.01	0.01
X	*3.01*			*3.03*	*2.98*	*3.01*	*3.00*
Fe^{3+}	1.41			0.90	0.90	1.04	1.79
Ti^{4+}	0.56			1.06	0.71	0.94	0.20
Cr^{3+}	0.01				0.38		
V^{3+}	0.01			0.01		0.01	0.01
Zr				0.01	0.02		
Y	*1.99*			*1.98*	*2.01*	*1.99*	*2.00*
Si	2.44			1.96	2.24	2.09	2.79
Al	0.21			0.23	0.29	0.27	0.14
Fe^{3+}	0.35			0.80	0.48	0.64	0.07
Z	*3.00*			*2.99*	*3.01*	*3.00*	*3.00*
Adr *	*72*			*49*	*62*	*55*	*89*
Sch	*17*			*40*	*24*	*32*	*4*
Htc	*11*			*11*	*14*	*13*	*7*

Adr * = andradite+uvarovite, Sch = schorlomite, Htc = hatcheonite.

Kalsilite is unevenly developed in paralavas and usual contains Na and Fe^{3+} impurities (Table 9, analyses 1,2). Kalsilite and products of its alteration (zeolites and Ca-hydrosilicates) are practically always noted in enclaves in association with walstromite and zadovite (Figure 3B,D). Very seldom, nepheline appears together with Ba-minerals (Table 9, analysis 3).

In walstromite-bearing paralava fluorapatite with high $(SiO_4)^{4-}$ content and non-stoichiometric formula $(Ca_{4.96}Sr_{0.03}Ba_{0.01})_{\Sigma 5.00}[(PO_4)_{2.66}(SiO_4)_{0.24}(SO_4)_{0.08}(VO_4)_{0.02}]_{\Sigma 3}F_{0.88}$ (Table 10, analysis 1) is widespread. For these grains, different charge balance schemes are considered. When $(SiO_4)^{4-}$ groups enter the fluorapatite structure the charge balance could be accomplished according to the ellestadite scheme of substitution—$2(PO_4)^{3-} \rightarrow (SiO_4)^{4-} + (SO_4)^{2-}$. But in this system is $(SO_4)^{2-}$ deficient. Raman spectroscopy investigation points out on the absence of significant content of $(CO_3)^{2-}$ groups, which might balance a lack of the sulphate group according to $2(PO_4)^{3-} \rightarrow (SiO_4)^{4-} + (CO_3)^{2-}$. We suspect, that charge balance of this apatite preserved by partial occupancy of the fluorine (Table 10, analysis 1).

Low-vanadium zadovite, $Ba(Ca_{5.81}Na_{0.18})_{\Sigma 5.99}[(SiO_4)_{0.86}(PO_4)_{1.14}]_{\Sigma 2.00}[(PO_4)_{1.86}(VO_4)_{0.10}(SO_4)_{0.05}]_{\Sigma 2.01}(F_{0.97}O_{0.03})_{\Sigma 1.00}$ (Table 10, analysis 2) and K-P-bearing gurimite, $(Ba_{2.67}K_{0.19}Ca_{0.11}Na_{0.02})_{\Sigma 3.02}[(VO_4)_{1.25}(PO_4)_{0.51}(SO_4)_{0.18}(SiO_4)_{0.03}(AlO_4)_{0.01}]_{\Sigma 1.98}$ (Table 10, analysis 3) crystallized before walstromite (Figure 3).

Table 8. Chemical composition of Ca-silicates from Zuk Tamrur (1, 3, 5) and Gurim Anticline paralava (2, 4, 6), wt.%.

| | 1 | | | 2 | | | 3 | | | 4 | | | 5 | | | 6 | | |
| | Rankinite | | | | | | cuspidine | | | | | | wollastonite | | | | | |
	n = 14	s.d.	Range	n = 18	s.d.	Range	N z = 6	s.d.	Range	n = 6	s.d.	Range	n = 9	s.d.	Range	n = 10	s.d.	Range
P_2O_5	0.16	0.08	0.04–0.38	0.14	0.04	0.03–0.22	0.16	0.04	0.10–0.20	n.d.			n.d.			n.d.		
TiO_2	n.d.			n.d.			n.d.			n.d.			0.21	0.15	0.01–0.47	n.d.		
SiO_2	40.82	0.26	40.33–41.23	41.34	0.19	40.94–41.66	31.86	0.68	30.87–32.47	32.39	0.19	32.02–32.66	50.77	0.94	48.09–51.52	51.78	0.51	51.25–52.85
Al_2O_3	n.d.			n.d.			0.04	0.10	0.00–0.22	n.d.			0.14	0.34	0.00–1.10	0.09	0.07	0.01–0.20
BaO	0.15	0.11	0.05–0.32	n.d.			0.46	0.02	0.44–0.49	n.d.			n.d.			n.d.		
SrO	n.d.			n.d.			0.12	0.18	0.00–0.43	0.20	0.08	0.09–0.34	n.d.			n.d.		
FeO	0.08	0.11	0–0.44	0.18	0.04	0–0.22	0.13	0.07	0–0.28	n.d.			0.12	0.06	0–0.22	0.17	0.08	0–0.30
CaO	57.61	0.38	56.81–58.17	57.48	0.34	56.78–57.98	59.37	0.69	58.53–60.01	60.33	0.60	59.40–61.10	48.16	0.60	46.89–49.09	48.10	0.13	47.67–48.13
MgO	0.06	0.02	0.03–0.11	0.05	0.02	0.02–0.08	0.03	0.01	0.03–0.04	n.d.			n.d.			n.d.		
K_2O	0.04	0.08	0.00–0.22	n.d.			n.d.			n.d.			n.d.			n.d.		
Na_2O	0.09	0.04	0.05–0.20	0.07	0.02	0.01–0.11	0.12	0.04	0.06–0.18	n.d.			n.d.			n.d.		
F	n.d.			n.d.			9.20	0.26	8.84–9.53	10.07	0.32	9.44–10.41	n.d.			n.d.		
H_2O							0.45			0.08								
–F=O							3.87			4.24								
Total	99.01			99.26			98.061			98.83			99.40			100.14		
Calculated on 7O *, 9(O + F + OH) ♣, 3O ♦																		
Ca	3.00 *			2.98 *			3.97 ♣			3.99 ♣			1.01 ♦			1.00 ♦		
Ba							0.01											
Sr										0.01								
Fe^{2+}				0.01			0.01											
Na	0.01			0.01			0.01											
A	*3.01*			*3.00*			*4.00*			*4.00*			*1.01*					
Si	1.98			2.00			1.99			2.00			0.99			1.00		
P^{5+}	0.01			0.01			0.01											
T	*1.99*			*2.01*			*2.00*			*2.00*			*0.99*			*1.00*		
F^-							1.81			1.97								
$(OH)^-$							0.19			0.03								
W							*2.00*			*2.00*								

Table 9. Chemical composition of kalsilite from Zuk Tamrur (1) and Gurim Anticline (2) and nepheline from Gurim Anticline (3).

	1			2			3
	n = 7	s.d.	Range	n = 6	s.d.	Range	n = 5
SiO_2	36.93	0.39	36.46–37.44	36.87	0.41	36.74–37.91	40.50
Fe_2O_3	4.56	1.39	2.84–6.38	4.56	0.62	3.50–5.38	3.37
Al_2O_3	27.89	1.48	26.08–29.82	27.97	0.56	26.87–28.30	32.06
BaO	0.75	0.60	0.11–1.72	1.33	0.61	0.62–2.37	n.d.
CaO	0.15	0.28	0.00–0.77	n.d.			0.07
MgO	0.09	0.09	0.00–0.25	0.12	0.06	0.03–0.22	n.d.
K_2O	26.57	1.20	25.22–27.89	27.03	0.46	26.30–27.42	8.91
Na_2O	1.53	0.48	0.98–2.28	0.96	0.11	0.69–0.98	15.02
Total	98.47			98.84			99.93
	Calculated on 4O						
K	0.92			0.94			0.28
Na	0.08			0.05			0.72
Ba	0.01			0.01			
A	*1.01*			*1.00*			*1.00*
Al	0.89			0.90			0.93
Fe^{3+}	0.09			0.09			0.06
Si	1.00			1.00			1.00
T	*1.98*			*1.99*			*1.99*

Table 10. Chemical composition of apatite (1, Zuk Tamrur), zadovite (2, Zuk Tamrur) and gurimite (3, Gurim Anticline).

	1			2	3
	n = 7	s.d.	Range	n = 4	n = 1
SO_3	1.29	0.2	1.11–1.69	0.49	2.38
V_2O_5	0.39	0.11	0.2–50.56	1.14	18.96
P_2O_5	37.47	0.53	38.37–39.66	27.80	6.07
SiO_2	2.84	0.27	2.61–3.33	6.73	0.26
Al_2O_3	n.d.			n.d.	0.08
BaO	0.42	0.13	0.32–0.71	20.01	68.12
SrO	0.54	0.20	0.44–0.98	n.d.	0.00
CaO	55.1	0.34	55.63–56.43	42.48	1.06
K_2O	n.d.			n.d.	1.53
Na_2O	n.d.			0.73	0.24
F	3.30	0.07	3.49–3.67	2.41	n.d.
-O=F	1.39			1.01	
Total	99.97			100.78	98.7
	Calculated on 8 Cations *, 17(O + F) ♣, 8O ♦				
Ba	0.0 *			1.00 ♣	2.67 ♦
Ca	4.96			5.81	0.11
Na				0.18	0.05
K					0.19
Sr	0.03				
A	*5.00*			*6.99*	*3.02*
Si	0.24			0.86	0.03
Al					0.01
P^{5+}	2.66			3.00	0.51
V^{5+}	0.02			0.10	1.25
S^{6+}	0.08			0.05	0.18
T	*3.00*			*4.01*	*1.98*
F	0.88			0.97	

4.2. Raman Spectroscopy

The Raman spectrum of walstromite from Israel is analogous to the spectrum of walstromite from Big Creek deposit, Fresno County, California [45] and exhibits common features with the spectra of isostructural margarosanite and breyite and also pseudowollastonite (Figure 4).

The main bands in the Raman spectra of walstromite, margarosanite, breyite and pseudowollastonite are related to vibrations of the $(Si_3O_9)^{6-}$ three-membered rings [46–49]. The band from Si-O-Si symmetric stretching vibrations in minerals of the margarosanite group are about 650–660 cm^{-1}, whereas in pseudowollastonite—at 580 cm^{-1} (Figure 4). That is connected with the distinct value of the Si-O-Si angle in $(Si_3O_9)^{6-}$ rings, extending from of 121.2–125.6° in walstromite, 120.2–123.3° in margarosanite, 123–123.9° in breyite to 134.45–134.65° in pseudowollastonite [13,32,50]. Bands from symmetric stretching vibrations of Si-O (apical oxygen) vibrations in all these minerals is roughly at the same position, in the interval 965–988 cm^{-1} (Figure 4). In the Raman spectrum of margarosanite taken from RRUFF database [51] this band has a relatively small intensity but then band about 1013 cm^{-1}, which is absent in the spectra of the other compared minerals, is the most intensive (Figure 4). This band has an unclear nature and needs in further investigation. Bands in range of 400–600 cm^{-1} in minerals of the margarosanite group and bands at 505 and 558 cm^{-1} in pseudowollastonite in principle are responded to bending vibrations of Si-O-Si and O-Si-O, whereas Ca-O, Ba-O and Pb-O vibrations have the main contribution in bands below 400 cm^{-1} [46,49]. The band below 1000 cm^{-1} is related to Si-O stretching antisymmetric vibrations in rings $(Si_3O_9)^{6-}$.
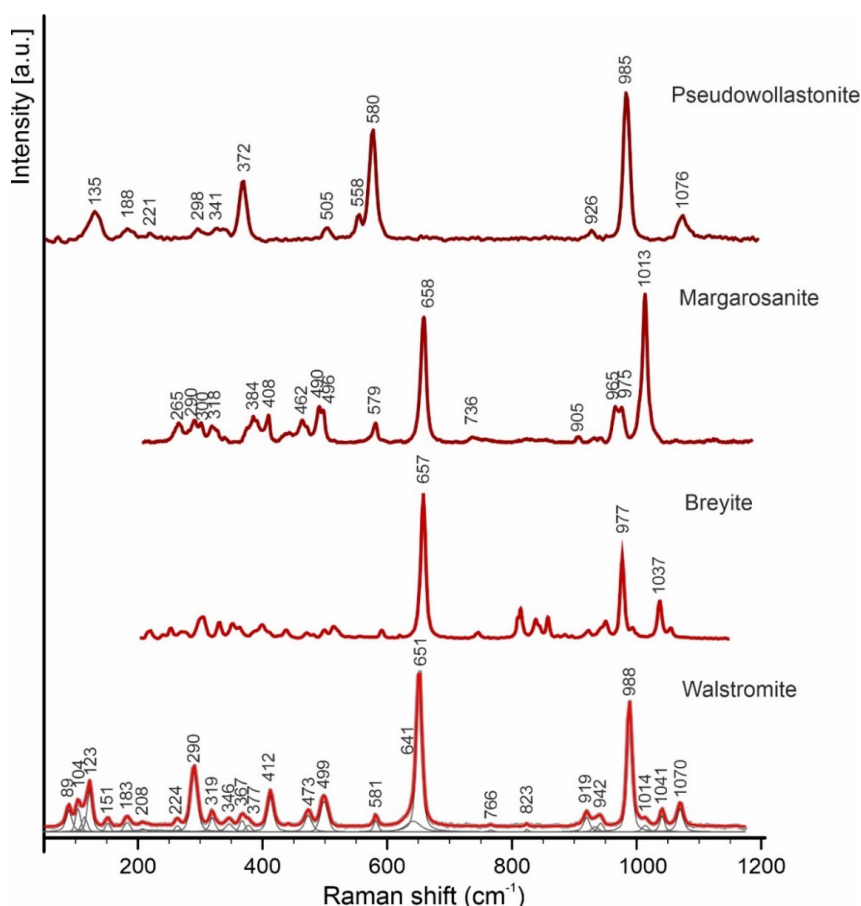
Figure 4. Raman spectra of walstromite from paralava of the Gurim Anticline and breyite (Anzolini et al., 2018 [16], excitation line 532 nm), margarosanite from Parker shaft, Franklin, NJ, USA (RRUFF, 532 nm) and pseudowollastonite-2M from gehlenite hornfels of the Negev Desert (488 nm).

4.3. Single-Crystal X-ray Diffraction Data

The structure of walstromite from Zuk Tamrur ($P\bar{1}$, $a = 6.7487(1)$Å, $b = 9.6292(1)$ Å, $c = 6.6999(1)$ Å, $\alpha = 69.658(1)°$, $\beta = 102.345(1)°$, $\gamma = 96.878(1)°$, V = 398.31(1) Å^3; Tables 1–4) is equivalent to the structure of holotype walstromite from Fresno, California ($P\bar{1}$, $a = 6.7335(2)$ Å, $b = 9.6142(2)$ Å, $c = 6.6859(2)$ Å, $\alpha = 69.638(2)°$, $\beta = 102.281(2)°$, $\gamma = 96.855(2)°$, V = 396.01(2) Å3) [15].

In the structure of walstromite, three-membered rings $(Si_3O_9)^{6-}$ intercalate with layers made of $Ca1O_8$ and $Ca2O_6$ polyhedra parallel to [101] (Figure 5A–D). The apices of the SiO_4 tetrahedra in neighboring rings are pointing in opposite directions (up or down). In addition, corrugated chains of edge-shared BaO_{10} polyhedra are running through the structure along the axis.

The three-membered rings $(Si_3O_9)^{6-}$, are formed by highly distorted SiO_4 tetrahedra with bond lengths between 1.576(2) and 1.689(2) Å. Typical for this configuration, the interatomic distances between Si and bridging oxygen of the ring (Si-O-Si) are longer (ca. 1.67–1.68 Å). Si-O bonds connecting the tetrahedra (and ring) with other polyhedra in the structure are shorter and are varying between 1.576(2) and 1.600(2) Å. Still, the average bond lengths of the SiO_4 tetrahedra are ca. 1.63 Å. The very same values have been reported by Barkley, Dows & Yang for another genetic type of walstromite found in Fresno, California.

In the Ca-layers, two $Ca1O_8$ and two $Ca2O_6$ polyhedra are sharing edges, building the Ca_4O_{20} blocks, which are further connected by shared edges to form a two-dimensional network (Figure 5D). The atom Ca1 is 6 + 2 coordinated and forms antiprism with Ca-O distance in the range of 2.33–2.85 Å (Table 4). Ca2 coordinated by 6 oxygens exhibits deformed octahedra with a mean distance Ca-O = 2.38 Å (Table 4). The chains of edge-sharing Ba-polyhedron, has 6 + 4 coordination with Ba1-O distance range of 2.563(2)–3.354(2) Å, with four bonds longer than 2.94 Å and mean distance of 2.943 Å (Table 4).
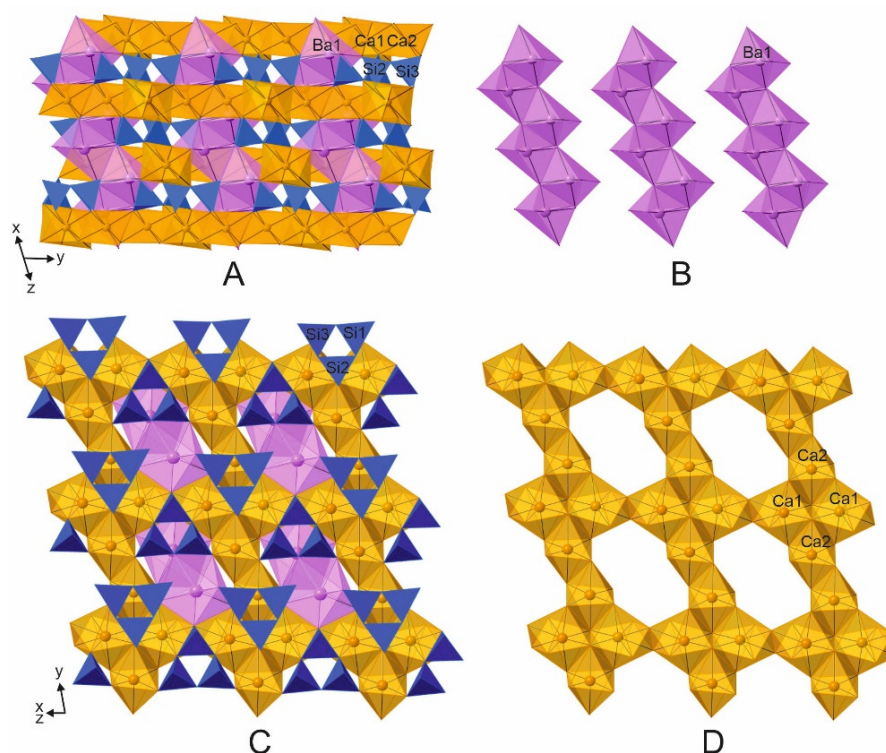
Figure 5. (**A**) Walstromite structure is formed by intercalation of tetrahedral layers built up by three-membered rings $(Si_3O_9)^{6-}$ with Ca-polyhedra layers. (**B**) In channels subperpendicular to layers there are Ba-polyhedra columns. (**C**) In tetrahedral layers $(Si_3O_9)^{6-}$ rings are alternately oriented up and down. (**D**) In Ca-polyhedra layers Ca_4O_{20} clusters are distinguished. Ca polyhedral: yellow-brown, Si-tetrahedra: blue, Ba-polyhedra: purple. Oxygens at the tops of polyhedral are not shown.

5. Discussion

For walstromite and its synthetic analogue, the unit cell parameters are given in the two different settings of the $P\bar{1}$ space group. In the earliest work by Glasser and Dent Glasser (1961) [52] the following parameters: $a \approx 6.72$ Å, $b \approx 6.73$ Å, $c \approx 9.62$ Å, $\alpha \approx 88°$, $\beta \approx 111°$, $\gamma \approx 102°$, were specified for $BaCa_2(Si_3O_9)$. In the later works, the other settings were used with unit cell parameters: $a \approx 6.74$ Å, $b \approx 9.61$ Å, $c \approx 6.69$ Å, $\alpha \approx 69°$, $\beta \approx 102°$, $\gamma \approx 97°$ [1,15,41,53]. This setting was taken as a base for the structure refinement of walstromite from Israel (Table 1). Walstromite, margarosanite and breyite belong to the structural type of the ring silicates with the three-membered rings $(Si_3O_9)^{6-}$ and general formula $AB_2(Si_3O_9)$ (Figure 6A–D) [13–15,50,52,53].
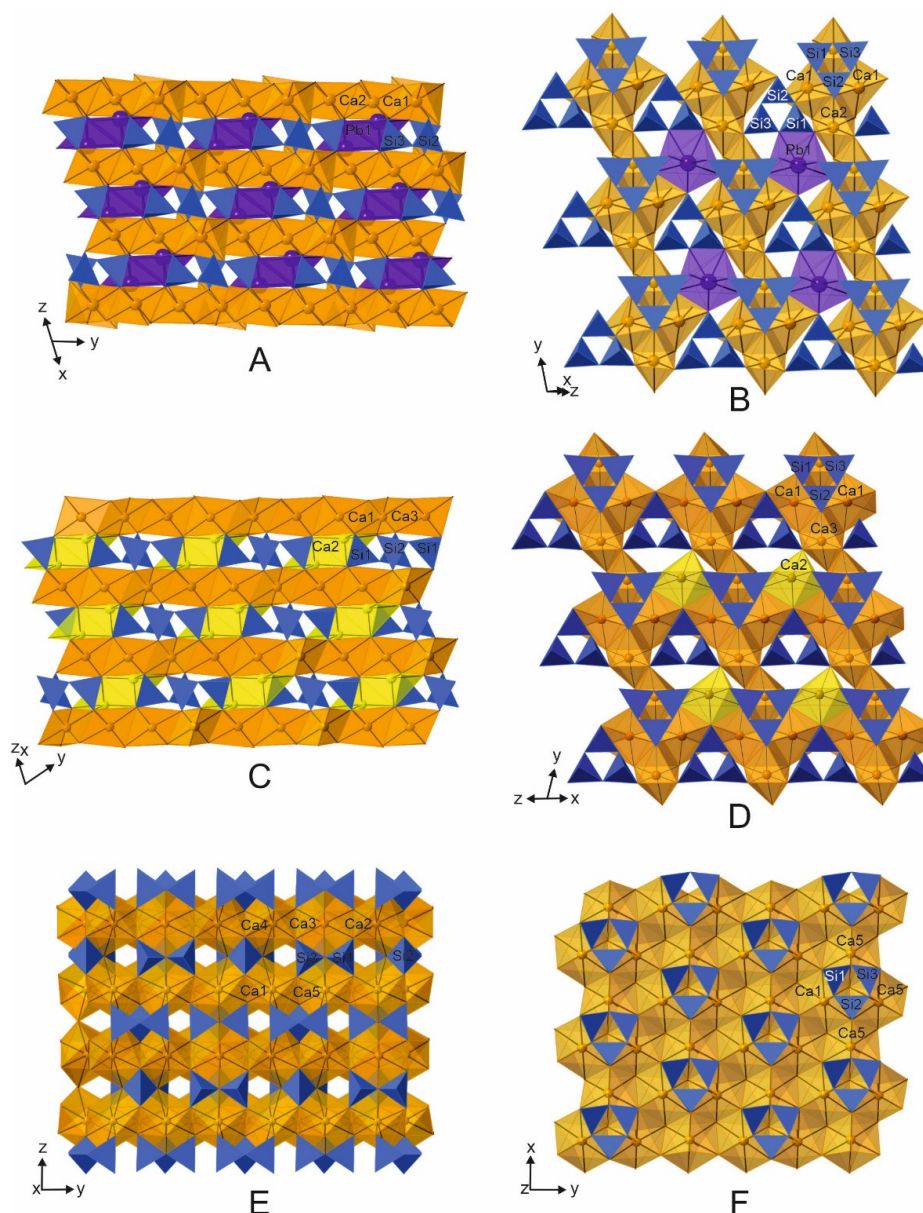
Figure 6. Crystal structures of margorosnite, $PbCa_2(SiO_3)_3$ (**A,B**) [50], breyite, $Ca_3(SiO_3)_3$ (**C,D**) [14] and pseudowollastonite-2*M*, $Ca_3(SiO_3)_3$ (**E,F**) [32]. Ca polyhedra: yellow-brown, Si-tetrahedra: blue, Pb-polyhedra: violet, Ca2 polyhedra (breyite): yellow. Oxygens at the tops of polyhedral are not shown.

A site is occupied by big two-valent cations—Ba (walstromite), Pb (margarosanite); B site is occupied by Ca. Breyite is an exception, both sites in which are occupied by Ca. Breyite, $Ca_3(Si_3O_9)$,

was described by Brenker from Ca-silicate inclusions trapped in a diamond coming from Juina, Brazil in 2018 [18]. It is a phase of high pressure, synthetic analogues of which were known before "wollastonite-II" or "Ca-walstromite" [15]. Margarosanite, $Pb(Ca,Mn^{2+})_2(Si_3O_9)$, was described by Ford and Bradley in 1916, from Franklin, Sussex County, NJ, USA [19]. Breyite is a wollastonite and pseudowollastonite polymorph. Pseudowollastonite, as well as minerals of the margarosanite group, has layered structure characterized by intercalation of layers formed by Ca-polyhedra with coordination 8 (deformed cubes) and tetrahedral layers formed by three-membered identically oriented $(Si_3O_9)^{6-}$ rings (Figure 6E, F) [32]. In breyite as in walstromite and margarosanite tetrahedral layer is formed by $(Si_3O_9)^{6-}$ ring, which are alternately oriented in opposite sides (Figure 6D) [49,50].

In the margarosanite group, the main distinctions in structure are observed for the coordination of A site, which is labelled as Ca2 in breyite [15]. In breyite Ca2 has coordination 6, at that site cation has an untypical position located in the plane of the deformed antiprism base (Figure 7A). Bigger Pb in margarosanite has coordination 6 + 1 (the next nearest oxygen is located at the distance ~3.5 Å) (Figure 7B). The bigger cation Ba in walstromite has coordination 6 + 4 (Figure 7C). Only in walstromite Ba polyhedra form columns along the c axis (Figure 5A,B), whereas in breyite and margarosanite Ca2 and Pb polyhedra form dimers (Figure 6A,C) [49,50].
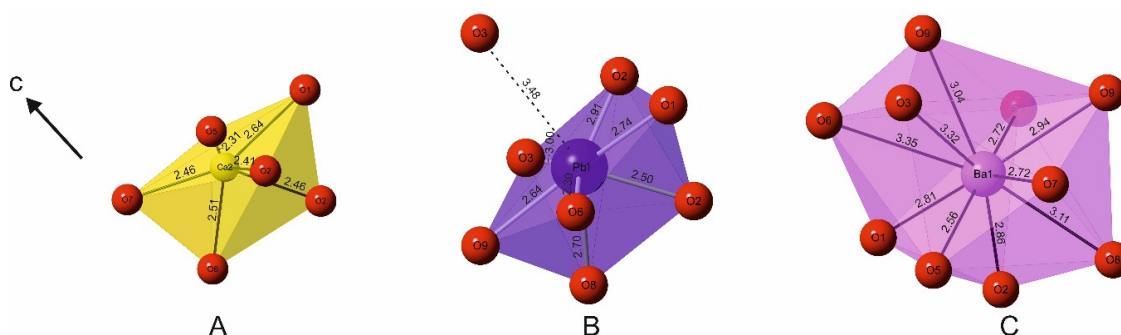
Figure 7. Polyhedra geometry Ca2 in breyite (**A**), Pb1 in margarosanite (**B**) and Ba1 in walstromite (**C**).

The genesis of unusual barium mineralization in rankinite paralava of the Hatrurim Basin was discussed by us before in the paper on gurimite and hexacelsian [11]. Basically, a genetic model of enclaves with Ba-mineralization formation sequence in rankinite paralavas can be described by the three stages:

I stage—melt formation.

Crystallization of gehlenite horfelses in the processes of pyrometamorphism is accompanied by the formation of a small amount of silicate melt. This silicate melt is translocated for a short distance and filled cracks in hornfelses.

II stage—crystallization of residual melt with the formation of rock-forming minerals.

Relatively quick crystallization of rock-forming minerals from melt begin from cracks walls on already existing crystal seeds (grains of early formed minerals of hornfelses) and comply with geometric selection during the growth, that leads to the formation of elongated crystals sub-perpendicular to the crack walls. Rock-forming minerals of paralava and hornfels are similar: andradite, gehlenite, wollastonite, rankinite, flamite-larnite, magnesioferrite and kalsilite. However, the size of the rock-forming minerals in paralava is 10–100 times bigger, than in hornfels.

III stage—formation of Ba-mineralization.

Quick crystallization of rock-forming minerals of paralava leads to the formation of enclaves with residual melt portions. This melt became enriched in Ba, V, P, S, Ti, U, K, F and other incompatible with rock-forming minerals chemical elements. From these melt specific aggregates (enclaves) with Ba-bearing minerals form. The size of these aggregates does not usually exceed the first millimeters. There are differences in the mineral specialization of similar enclaves. For instance, minerals of the

zadovite-aradite series, walstromite and gurimite are not associated with barioferrite and perovskite (titanian specialization) [34].

Detection of pseudowollastonite in rankinite paralava can indicate that the temperature peak of rock formation is higher than 1100 °C [32]. We tested a big number of phases with composition $CaSiO_3$ from walstromite-bearing paralava from Zuk Tamrur and Gurim Anticline and did not identify neither the one pseudowollastonite crystal. Eutectic intergrowings of walstromite with kalsilite (Figure 3C) and frequent findings of cuspidine in close contact with it point out its crystallization from the melt enriched in potassium (+sodium) and fluorine, which has an effect on the reduced temperature of walstromite crystallization. In metakaolin-waste glass geopolymers enriched in NaOH walstromite appears at a temperature about 600 °C [54].

We consider that the temperature of walstromite formation was significantly lower than 1000 °C.

Conflicts of Interest: The authors declare no conflict of interest.

References

1. Alfors, J.T.; Stinson, M.C.; Matthews, R.A.; Pabst, A. Seven new barium minerals from eastern Fresno County, California. *Am. Mineral.* **1965**, *50*, 314–340.

2. Dunning, G.; Cooper, J.K., Jr. Barium silicate minerals from Trumbull Peak, Mariposa County, California. *Mineral. Rec.* **1999**, *30*, 411–417.

3. Walstrom, R.E.; Dunning, G.E. The Baumann prospect Chickencoop Canyon, Tulare County California. *Mineral. Rec.* **2003**, *34*, 159–166.

4. Dunning, G.E.; Walstrom, R.E.; Lechner, W. Barium silicate mineralogy of the western margin, North American Continent, Part 1: Geology, origin, paragenesis and mineral distribution from Baja California Norte, Mexico, western Canada and Alaska, USA. *Baymin J.* **2018**, *19*, 1–70.

5. McNeil, L.A.; Peterson, R.C.; Farber, G.; Groat, L.; Witzke, T. Mineralogical studies of a low-temperature hydrothermal barium-rich skarn deposit, Gunn Claim, Yukon Territory. In Proceedings of the Winnipeg 2013: GAC–MAC Joint Annual Meeting, Winnipeg, MT, Canada, 22–24 May 2013; Volume 135, p. 135.

6. Peterson, R.C.; Farber, G.; Evans, R.J.; Groat, L.; MacNeil, L.; Joy, B.; Lafuente, B.; Witzke, T. Meierite, a new barium mineral with a Kfi-type zeolite framework from the Gun Claim, Yukon Canada. *Can. Mineral.* **2016**, *54*, 1249–1259. [CrossRef]

7. Bentor, Y.K. *Lexique Stratigraphique International: Asie fascicule 10 c 2 Israel*; Centre National de la Recherche Scientifique: Paris, France, 1960; Volume 3.

8. Gross, S. The mineralogy of the Hatrurim Formation, Israel. *Geol. Surv. Isr. Bull.* **1977**, *70*, 1–80.

9. Novikov, I.; Vapnik, Y.; Safonova, I. Mud volcano origin of the Mottled Zone, South Levant. *Geosci. Front.* **2013**, *4*, 597–619. [CrossRef]

10. Galuskin, E.V.; Gfeller, F.; Galuskina, I.O.; Pakhomova, A.; Armbruster, T.; Vapnik, Y.; Włodyka, R.; Dzierżanowski, P.; Murashko, M. New minerals with a modular structure derived from hatrurite from the pyrometamorphic Hatrurim Complex. Part II. Zadovite, $BaCa_6[(SiO_4)(PO_4)](PO_4)_2F$ and aradite, $BaCa_6[(SiO_4)(VO_4)](VO_4)_2F$, from paralavas of the Hatrurim Basin, Negev Desert, Israel. *Min. Mag.* **2015**, *79*, 1073–1087. [CrossRef]

11. Galuskina, I.O.; Galuskin, E.V.; Vapnik, Y.; Prusik, K.; Stasiak, M.; Dzierżanowski, P.; Murashko, M. Gurimite, $Ba_3(VO_4)_2$ and hexacelsian, $BaAl_2Si_2O_8$—Two new minerals from schorlomite-rich paralava of the Hatrurim Complex, Negev Desert, Israel. *Min. Mag.* **2017**, *81*, 1009–1019. [CrossRef]

12. Krzątała, A.; Krüger, B.; Galuskina, I.; Vapnik, Y.; Galuskin, E. Bennesherite, IMA 2019-068; CNMNC Newsletter No. 52. *Min. Mag.* **2019**, *83*, 887–893.

13. Trojer, F.J. The crystal structure of a high-pressure polymorph of CaSiO₃. *Z. Kristallogr.* **1969**, *130*, 185–206. [CrossRef]

14. Werner, J.; Paulus, E.F.; Winkler, B.; Milman, V. The crystal structure of CaSiO₃-walstromite, a special isomorph of wollastonite-II. *Z. Kristallogr.* **2003**, *218*, 811–818.

15. Barkley, M.C.; Downs, R.T.; Yang, H. Structure of walstromite, $BaCa_2Si_3O_9$ and its relationship to CaSiO₃-walstromite and wollastonite-II. *Am. Mineral.* **2011**, *96*, 797–801. [CrossRef]

16. Anzolini, C.; Angel, R.J.; Merlini, M.; Derzsi, M.; Tokár, K.; Milani, S.; Krebs, M.Y.; Brenker, F.E.; Nestola, F.; Harris, J.W. Depth of formation of CaSiO₃-walstromite included in super-deep diamonds. *Lithos* **2016**, *265*, 138–147. [CrossRef]

17. Anzolini, C.; Prencipe, M.; Alvaro, M.; Romano, C.; Vona, A.; Lorenzon, S.; Smith, E.M.; Brenker, F.E.; Nestola, F. Depth of formation of super-deep diamonds: Raman barometry of CaSiO₃-walstromite inclusions. *Am. Mineral.* **2018**, *103*, 69–74. [CrossRef]

18. Brenker, F.; Nestola, F.; Brenker, L.; Peruzzo, L.; Secco, L.; Harris, J.W. Breyite, IMA 2018-062, CNMNC Newsletter No. 45, October 2018, page 1041. *Eur. J. Mineral.* **2018**, *30*, 1037–1043.

19. Ford, W.E.; Bradley, W.M. Margarosanite, a new lead-calcium silicate from Franklin, N.J. *Am. J. Sci.* **1916**, *42*, 159–162. [CrossRef]

20. Britvin, S.N.; Murashko, M.N.; Vapnik, Y.; Polekhovsky, Y.S.; Krivovichev, S.V. Earth's Phosphides in Levant and insights into the source of Archean prebiotic phosphorus. *Sci. Rep.* **2015**, *5*, 8355. [CrossRef]

21. Vapnik, Y.; Sharygin, V.V.; Sokol, E.V.; Shagam, R. Paralavas in a combustion metamorphic complex: Hatrurim Basin, Israel. In *Geology of Coal Fires: Case Studies from Around the World*; Geological Society of America: Boulder, CO, USA, 2007; Volume 18, pp. 133–153. ISBN 978-0-8137-4118-5.

22. Galuskina, I.O.; Vapnik, Y.; Lazic, B.; Armbruster, T.; Murashko, M.; Galuskin, E.V. Harmunite $CaFe_2O_4$—A new mineral from the Jabel Harmun, West Bank, Palestinian Autonomy, Israel. *Am. Mineral.* **2014**, *99*, 965–975. [CrossRef]

23. Sokol, E.; Novikov, I.; Zateeva, S.; Vapnik, Y.; Shagam, R.; Kozmenko, O. Combustion metamorphism in the Nabi Musa dome: New implications for a mud volcanic origin of the Mottled Zone, Dead Sea area. *Basin Res.* **2010**, *22*, 414–438. [CrossRef]

24. Kolodny, Y.; Burg, A.; Sneh, A. Comment on Combustion metamorphism (CM) in the Nabi Musa dome: New implications for a mud volcanic origin of the Mottled Zone, Dead Sea area, by: E.Sokol, I.Novikov, S.Zateeva, Ye.Vapnik, R. Shagamand O.Kozmenko, Basin Research (2010) 22, 414–438. *Basin Res.* **2013**, *25*, 112–114. [CrossRef]

25. Vapnik, Y.; Novikov, I. Reply to Comment of Y. Kolodny, A. Burg and A. Sneh on "Combustion metamorphism in the Nabi Musa dome: New implications for a mud volcano origin of the Mottled Zone, Dead Sea area," by E. Sokol, I. Novikov, S. Zateeva, Ye. Vapnik, R. Shagam and O. Kozmenko, Basin Research (2010), 22, 414–438. *Basin Res.* **2013**, *25*, 115–120.

26. Picard, l. *Geological Research in the Judean Desert*; Goldberg's Press: Jerusalem, Israel, 1931; p. 108.

27. Minster, T.; Yoffe, O.; Nathan, Y.; Flexer, A. Geochemistry, mineralogy and paleoenvironments of deposition of the Oil Shale Member in the Negev. *Isr. J. Earth Sci.* **1997**, *46*, 41–59.

28. Burg, A.; Starinsky, A.; Bartov, Y.; Kolodny, Y. Geology of the Hatrurim Formation ("Mottled Zone") in the Hatrurim Basin. *Isr. J. Earth Sci.* **1991**, *40*, 107–124.

29. Burg, A.; Kolodny, Y.; Lyakhovsky, V. Hatrurim-2000: The "Mottled Zone" revisited, forty years later. *Isr. J. Earth Sci.* **2000**, *48*, 209–223.

30. Sokol, E.V.; Kozmenko, O.A.; Kokh, S.N.; Vapnik, Y. Gas reservoirs in the Dead Sea area: Evidence from chemistry of combustion metamorphic rocks in Nabi Musa fossil mud volcano. *Russ. Geol. Geophys.* **2012**, *3*, 745–762. [CrossRef]

31. Fishman, I.L.; Kazakova, Y.I.; Sokol, E.V.; Stracher, G.B.; Kokh, S.N.; Polyansky, O.P.; Vapnik, Y.; White, Y.; Bajadilov, K.O. Mud volcanism and gas combustion in the Yli Depression, Southeastern Kazakhstan. In *Coal and Peat Fires: A Global Perspective, Vol. 2: Photographs and Multimedia Tours*; Stracher, G.B., Prakash, A., Sokol, E.V., Eds.; Elsevier: Amsterdam, The Netherlands, 2012; Volume 2, pp. 217–231; ISBN 978-0-444-59412-9.

32. Seryotkin, Y.V.; Sokol, E.V.; Kokh, S.N. Natural pseudowollastonite: Crystal structure, associated minerals and geological context. *Lithos* **2012**, *134*, 75–90. [CrossRef]

33. Sharygin, V.V.; Sokol, E.V.; Vapnik, Y. Minerals of the pseudobinary perovskite-brownmillerite series from combustion metamorphic larnite rocks of the Hatrurim Formation (Israel). *Russ. Geol. Geophys.* **2008**, *49*, 709–726. [CrossRef]

34. Krząłała, A.; Panikorovskii, T.; Galuskina, I.; Galuskin, E. Dynamic Disorder of Fe^{3+} Ions in the Crystal Structure of Natural Barioferrite. *Minerals* **2018**, *8*, 340. [CrossRef]

35. Gfeller, F.; Widmer, R.; Krüger, B.; Galuskin, E.V.; Galuskina, I.O.; Armbruster, T. The crystal structure of flamite and its relation to Ca_2SiO_4 polymorphs and nagelschmidtite. *Eur. J. Mineral.* **2015**, *27*, 755–769. [CrossRef]

36. Waltersperger, S.; Olieric, V.; Pradervand, C.; Glettig, W.; Salathe, M.; Fuchs, M.R.; Curtin, A.; Wang, X.; Ebner, S.; Panepucci, E.; et al. PRIGo: A new multi-axis goniometer for macromolecular crystallography. *J. Synchrotron. Radiat.* **2015**, *22*, 895–900. [CrossRef] [PubMed]

37. Wojdyla, J.A.; Kaminski, J.W.; Panepucci, E.; Ebner, S.; Wang, X.; Gabadinho, J.; Wang, M.J. DA+ data acquisition and analysis software at the Swiss Light Source macromolecular crystallography beamlines. *Synchrotron Rad.* **2018**, *25*, 293–303.

38. Rigaku. *CrysAlisPro*; Rigaku Oxford Diffraction Ltd.: Yarnton, UK, 2016.

39. Sheldrick, G.M. A short history of SHELX. *Acta Crystallogr.* **2008**, *A64*, 112–122. [CrossRef] [PubMed]

40. Farrugia, L.J. WinGX suite for small-molecule single-crystal crystallography. *J. Appl. Crystallogr.* **1999**, *32*, 837–838. [CrossRef]

41. Glasser, L.S.D.; Glasser, F.P. The crystal structure of walstromite. *Am. Mineral.* **1968**, *53*, 9–13.

42. Krząłała, A.; Galuskina, I.O. Potentially new mineral of the apatite group, Ba5(PO4)3F-fluorine analogue of alforsite from the Hatrurim complex, Israel. In Proceedings of the 200th Anniversary Meeting of the Russian Mineralogical Society, Saint-Petersburg, Russia, 10–13 October 2017; pp. 72–73.

43. Pekov, I.V.; Zubkova, N.V.; Koshlyakova, N.N.; Krząłała, A.; Belakovskiy, D.I.; Galuskina, I.O.; Galuskin, E.V.; Britvin, S.N.; Sidorov, E.G.; Vapnik, Y.; et al. Pliniusite, IMA 2018-031, CNMNC Newsletter No. 44, August 2018, page 881. *Eur. J. Mineral.* **2018**, *30*, 877–882.

44. Wiedenmann, D.; Zaitsev, A.N.; Britvin, S.N.; Krivovichev, S.V.; Keller, J. Alumoåkermanite, $(Ca,Na)_2(Al,Mg,Fe^{2+})(Si_2O_7)$, a new mineral from the active carbonatite-nephelinite-phonolite volcano Oldoinyo Lengai, northern Tanzania. *Min. Mag.* **2009**, *73*, 373–384.

45. Gaft, M.; Yeates, H.; Nagli, L. Laser-induced time-resolved luminescence of natural margarosanite $Pb(Ca,Mn)_2Si_3O_9$. Swedenborgite $NaBe_4SbO_7$ and walstromite $BaCa_2Si_3O_9$. *Eur. J. Mineral.* **2013**, *25*, 71–77. [CrossRef]

46. McKeown, D.A.; Bell, M.I.; Kim, C.C. Raman spectroscopy of silicate rings: Benitoite and the three-membered ring. *Phys. Rev. B* **1993**, *48*, 16357–16365. [CrossRef]

47. Sitarz, M.; Mozgawa, W.; Handke, M. Vibrational spectra of complex ring silicate anions—Method of recognition. *J. Mol. Struct.* **1997**, *404*, 193–197. [CrossRef]

48. Richet, P.; Mysen, B.O.; Ingrin, J. High-temperature X-ray diffraction and Raman spectroscopy of diopside and pseudowollastonite. *Phys. Chem. Mineral.* **1998**, *25*, 401–414. [CrossRef]

49. Takahashi, Y.; Iwasaki, K.; Masai, H.; Fujiwara, T. Raman spectroscopic study of benitoite-type compounds. *J. Ceram. Soc. Jpn.* **2008**, *116*, 1139–1142. [CrossRef]

50. Freed, R.L.; Peacor, D. Determination and refinement of the crystal structure of margarosanite, $PbCa_2Si_3O_9$. *Z. Kristallogr.* **1969**, *128*, 213–228. [CrossRef]

51. Lafuente, B.; Downs, R.T.; Yang, H.; Stone, N. The power of database: The RRUFF project. In *Highlights in Mineralogical Crystallography*; Armbruster, T., Danisi, R.M., Eds.; W. De Gruyter: Berlin, Germany, 2016; pp. 1–30.

52. Glasser, F.P.; Dent Glasser, L.S. Crystallographic study of $Ca_2BaSi_3O_9$. *Z. Kristallogr. Cryst. Mater.* **1961**, *116*, 263–265. [CrossRef]

53. Basciano, L.C. Mineralogy and Crystal Structures of Barium Silicate Minerals from Fresno County, California. Master's Thesis, The University of British Columbia, Vancouver, BC, Canada, 1999.

54. Moncea, M.A.; Panait, A.M.; Dumitru, F.D.; Baraitaru, A.G.; Olteanu, M.V.; Boboc, D.G.; Stanciu, S. Metakaolin—Waste glass geopolymers. The influence of hardening conditions on mechanical performances. *IOP Conf Ser. Mater. Sci. Eng.* **2019**, *572*, 012057. [CrossRef]